

Trajectory Optimization to Delay Turbulent Transition for Mars Entry Aeroshells

Roman Y. Jits⁽¹⁾ and David A. Saunders⁽²⁾

⁽¹⁾ELORET Corp., MS 230-2, NASA Ames Research Center, CA 94035, USA, Email: ryjits@gmail.com,

⁽²⁾ELORET Corp., MS 230-2, NASA Ames Research Center, CA 94035, USA, David.A.Saunders@NASA.gov

ABSTRACT

In a preparatory aeroshell shape optimization study of Mars Science Laboratory-class entry vehicles, the present authors found that an Apollo-like spherical-segment experiences significantly lower convective heating than the 70° sphere-cone of MSL during the descent phase. Other forebodies, axisymmetric or not, were also investigated, but for the ensuing trajectory studies summarized here, the Apollo-like shape was adopted. Higher L/Ds with fairly high C_D s permit wider entry corridors, reduced heating rates and dynamic pressures, and the potential to shape the entry trajectory in order to delay transition to turbulence. For some range of missions, the transition delay could enable more mass-efficient heat shield design by preserving laminar flow on a substantial portion of the forebody. A constraint based on the momentum thickness Reynolds number (Re_θ) obtained from real gas flow solutions was constructed in Velocity-Altitude space to span the flyable envelope as a lower bound during trajectory optimization with increasingly shallow entry angles and Mach 2.1 termination above 10 km altitude. Further optimizations in the presence of off-nominal factors demonstrated robustness of the approach, which (with adjustments from lessons learned) might also be applied to aerocapture trajectories for larger entry vehicles.

1. INTRODUCTION

Atmospheric entry vehicles for all Mars missions to date have employed forebodies with simple geometric shapes comprised of cones and spherical noses. The cone semi-angles were 70° for the Viking landers, Pathfinder, the Mars Exploration Rovers, Phoenix, and the Mars Science Laboratory aeroshells. The low density of the Martian atmosphere demands high drag in order to reduce relative entry speed from about 6 km/s or Mach 25 to around Mach 2 at about 10 km altitude (MSL figures), partly explaining the bluntest 70° choice for all of the Mars landers, except Beagle 2 (60°). While there is much to be said for adhering to heritage shapes with their accumulated databases of aerodynamic and aerothermal performance, the fact that the largest Martian lander so far (MSL at 4.5 m diameter) had its thermal protection system (TPS) material changed at the eleventh hour is one indication that the traditional sphere/cone is not ideal for further upward scaling.

With that in mind, the possibility of improving L/D (lift-to-drag ratio) over the approximate 0.24 limit for MSL without reducing the drag coefficient (C_D) too much was explored in terms of aeroshell shape

optimization [1]. An optimized aeroshell with a higher L/D for MSL-class missions would allow for greater flexibility in shaping the nominal trajectory to produce less severe aerothermal environments while meeting the same end conditions suitable for parachute deployment. Aeroshell configurations considered in this study were constrained to have the same diameter (4.5 m) as MSL, although they were allowed to become asymmetrical in the process of optimization. The conclusion, supported by real gas computational fluid dynamics (CFD) calculations, was that, among the shapes explored, asymmetry appeared not to provide enough benefits to justify the added complexity, while an Apollo-like forebody with better blending at the shoulder appeared to warrant consideration for future MSL-class Mars missions because of its lower (convective) heating. [Radiative heating becomes more of an issue for larger vehicles, especially at high entry speeds greater than 7 km/s.]

This paper presents results from optimizing Mars entry trajectories entering at the shallower angles permitted by the wider corridors associated with higher L/D and reasonably high C_D at higher angles of attack. The optimization turned from minimizing peak stagnation point heating to minimizing peak dynamic pressure as a more meaningful way of delaying transition to turbulent flow. More explicitly, a CFD-based constraint in Velocity-Altitude space was employed with the intent of preserving laminar flow over the upper half of the heat shield for the bulk of the entry, according to the criterion $Re_\theta < 200$ [2]. Following establishment of a nominal L/D = 0.39 trajectory, the effects of atmospheric and aerodynamic dispersions were studied by reoptimizing the trajectory in the presence of multiple off-nominal factors. CFD analysis at peak conditions along the worst resulting off-nominal trajectory confirmed the robustness of the nominal shallow trajectory.

Summaries of the *HEAT_SHIELD* shape optimization scheme and the *DPLR* real gas flow solver employed at NASA Ames Research Center are provided next for completeness, and construction of an Altitude-Velocity constraint is briefly outlined. Trajectory optimization at given L/D and C_D is then focused upon for the rest of the paper.

1.1 Shape Optimization Outline

The shape optimization study [1] applied nonlinear numerical optimization techniques using curvature-based constraints and modified Newtonian aerodynamics in conjunction with CFD analyses of candidate forebody configurations to investigate how a combination of shape and trajectory optimization for

MSL-class vehicles might overcome known limitations of the traditional 70° sphere-cone [3]. Controlling surface curvature (partly to avoid too-small radii and partly to follow bow shock curvature) allows indirect control of surface convective heating and tendency towards turbulent transition. A measure of volume-to-surface area can be maximized among other possible objective functions. Constraints on C_D and L/D and moment center can ensure viability of more benign entry trajectories. Use of families of perturbing shape functions applied along and across the initial defining spokes permits broad choice of shape, as opposed to using analytic shapes with fewer variables. Non-axisymmetric as well as axisymmetric geometries can be considered. In practice, progressively tightening the active constraint bounds leads to a sequence of optimized shapes. CFD analysis of the most promising results from this study showed that none satisfying all constraints appeared preferable to what turned out to be a large main section of constant (0.21 m^{-1}) curvature blended smoothly at the shoulder where the curvature met the specified upper bound of 6 m^{-1} —in other words, essentially the familiar heat shield shape of Apollo and the Orion Crew Exploration Vehicle.

Shape comparisons are beyond the present scope, but Fig. 1 shows this Apollo-like forebody overlaid on the MSL forebody, along with its modified Newtonian aerodynamics for a representative Mach number. Note the viable L/D values of interest highlighted in red beyond (blue) $L/D \approx 0.24$, which is the angle-of-attack-limited maximum for the 70° sphere-cone. Higher Alphas will be exploited.

1.2 Reacting Flow Solutions

Three-dimensional laminar and turbulent solutions for the real gas Navier-Stokes flow equations were calculated in this work using the *DPLR* flow solver [4] with an eight-species (CO_2 , CO , N_2 , O_2 , NO , C , N , O) finite-rate Mitcheltree chemistry model, including the effects of thermal nonequilibrium. *DPLR* employs a parallel multiblock finite volume algorithm that treats the Euler fluxes with a low-dissipation form of Steger-Warming flux vector splitting, third-order spatial accuracy, and second-order accuracy in the viscous flux central difference scheme.

Supercatalytic radiative equilibrium was specified at the wall, and the free stream species mass fractions used for the Martian atmosphere were 0.97088 CO_2 and 0.02912 N_2 . The turbulence model employed was the Menter-SST two-equation eddy-viscosity model with compressibility corrections.

Grid generation for analyzing forebody geometries from *HEAT_SHIELD* is performed via automated elimination of the singular apex point in the spoked surface grid, and scripted hyperbolic growth of an initial volume grid off the surface via *Gridgen* (Pointwise, Inc.). *DPLR* itself realigns the grid outer boundary with the shock envelope in several distinct steps until the surface heating is well converged.

Typical turn-around is a day or two using 56 or 112 processors on grids with 750,000+ cells.

1.3 Construction of Altitude-Velocity Constraint

For the chosen L/D of 0.39 permitted by the Apollo-like forebody, an angle of attack of -26° was specified and a matrix of 15 *DPLR* solutions was calculated at 5 velocities (5.5, 5, 4, 3, and 2 km/s) and judicious altitudes 2 km apart, three per velocity, covering the range 42-18 km altitude. Plotting where the vertical centerline coordinate showed $Re_\theta = 200$ on these five lines versus altitude allowed interpolation of 5 points corresponding to laminar flow at and above the apex. The trajectory solver can interpolate within that small dataset to impose a lower-bound constraint in Velocity-Altitude space (if only for the selected C_L and C_D).

Such a constraint, while planned for, was not in the picture during initial trajectory calculations at lower L/D s. The sequence of steps taken to develop a robust optimized trajectory for an MSL-class mission is outlined in the following sections.

2. NOMINAL TRAJECTORY DESIGN

Entry trajectories for this study were developed using *POST II* optimization capabilities [5], seeking a bank control schedule specific to each trajectory such that target end conditions were met while a specified parameter (for example, peak stagnation point heat flux, or maximum dynamic pressure) was minimized. For preliminary design purposes, three degrees of freedom simulation is sufficient and the angle of attack and aerodynamic coefficients can reasonably be considered constant with respect to hypersonic Mach number, as subsequent real gas flow calculations indeed largely justify, at least for the designs pursued. (Supersonic differences are also ignored.) A nominal atmosphere was used and no other off-nominal conditions were modeled at this stage.

The type of bank angle schedule specified for all trajectories is illustrated with a representative example in Fig. 2. Reasonable choices of 8 bank steps and 7 associated time intervals were adopted for the optimization variables, with instantaneous changes between steps. Zero degrees bank means full lift up. Angle of attack was held fixed for a given trajectory. Entry was at 137 km altitude with bank held at zero until 120 km altitude.

Entry corridors were developed for a range of L/D , starting from $L/D = 0.24$, as a reference to MSL trajectory performance, and for four other, progressively higher L/D values, with the highest $L/D = 0.39$; see Table 1. The entry vehicle was assumed to have a fixed mass of 2,918 kg and a reference area of 15.9043 m^2 . Undershoot and overshoot trajectories were developed to establish entry corridors, and they were targeted to parachute deployment conditions of Mach 2.1 above 10 km altitude. Initial nominal entry angles were set in the middle of the entry corridors, and nominal trajectories were similarly targeted. The mid-

corridor $L/D = 0.24$ trajectory was also optimized for minimum stagnation point heating (Fay-Riddell formulation [6]). Altitude time histories for all entry trajectories generated at $L/D = 0.24$ are shown in Fig. 3. As seen from Table 1, the higher L/D values yield wider entry corridor widths. This is advantageous as already noted because it allows more flexibility in

designing non-orthodox nominal trajectories customized for more benign aerothermal heating environments—for example, by optimizing the trajectory to delay likely transition to turbulent flow.

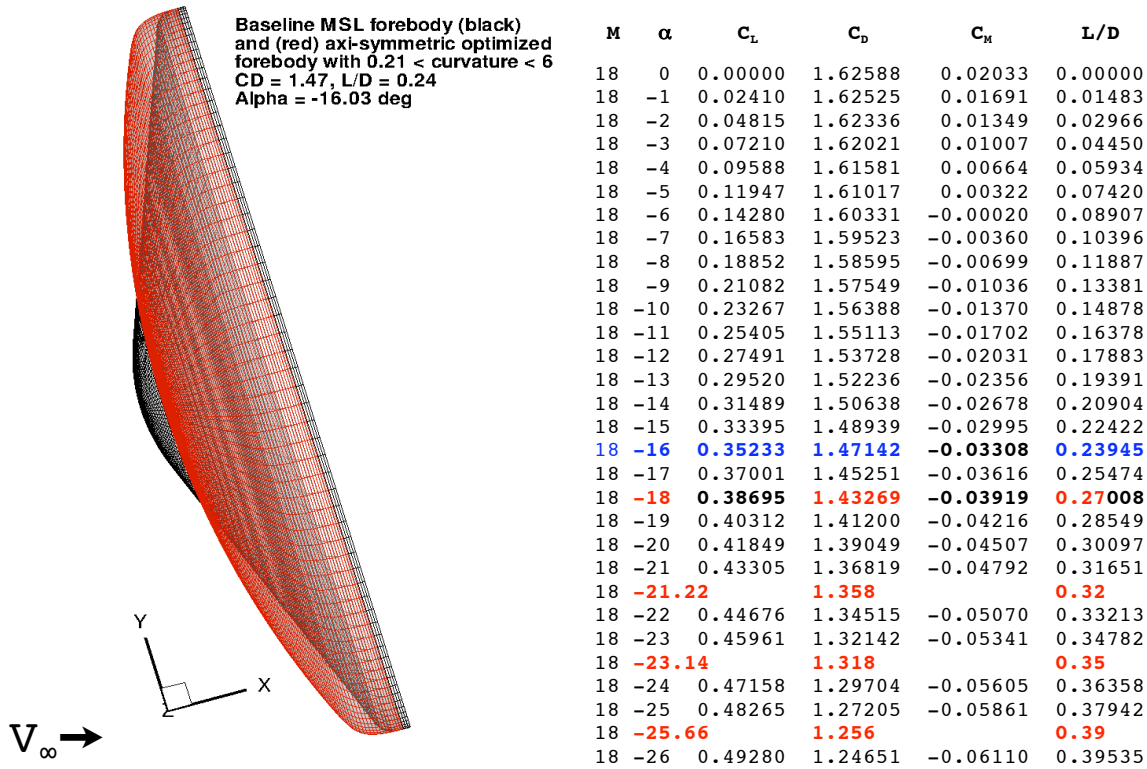


Fig. 1. Geometry comparison and Mach 18 modified Newtonian aerodynamics for optimized Apollo-like axisymmetric aeroshell, with L/D values of interest highlighted.

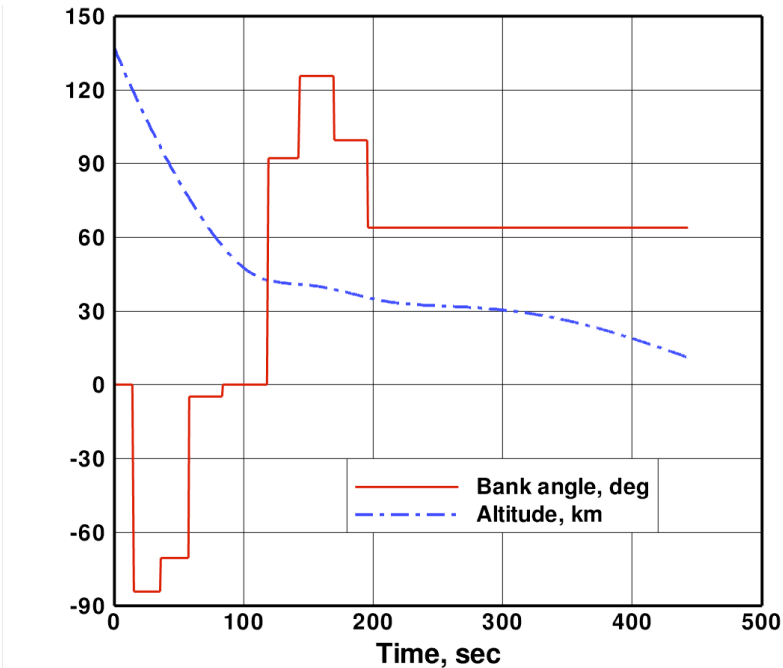
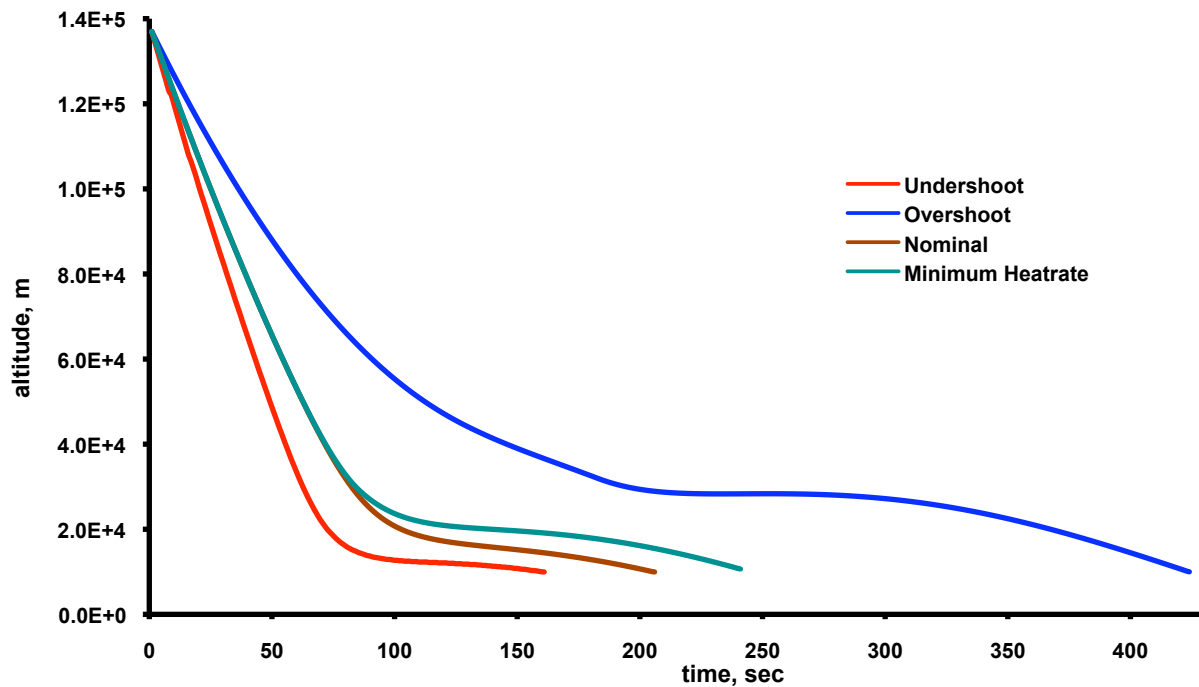


Fig. 2. Representative bank angle control schedule and associated altitude time history.

Table 1 Entry angles for overshoot, undershoot and nominal trajectories

L/D	Undershoot, deg	Overshoot, deg	Corridor Width, deg	Nominal, deg
0.24	-19.245	-11.33	7.915	-15.288
0.27	-19.50	-10.61	8.890	-15.055
0.32	-19.94	-10.43	9.510	-15.185
0.35	-20.36	-10.38	9.980	-15.370
0.39	-20.82	-10.44	10.380	-15.630

**Fig. 3. L/D = 0.24 trajectories: overshoot, undershoot, nominal, and optimized for minimum peak stagnation point heating rate according to the Fay-Riddell formulation.**

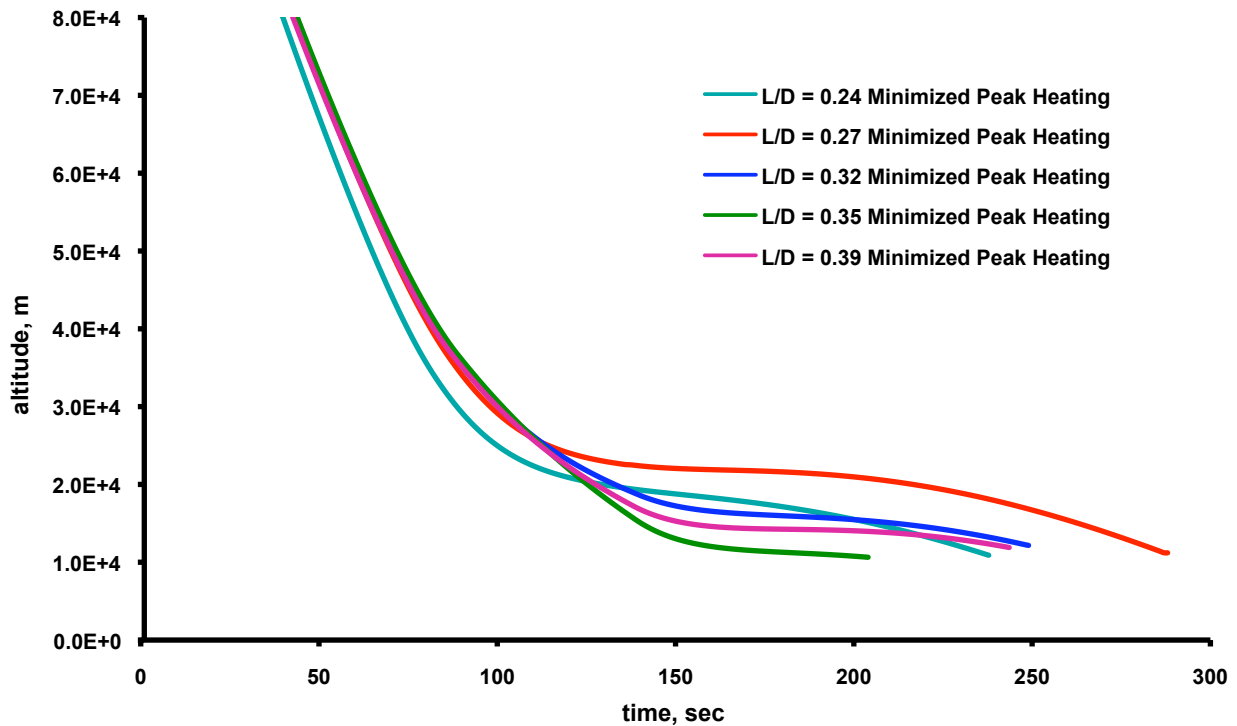
2.1 Design of Shallower Trajectories Optimized for Minimum Peak Stagnation Point Heating

Entry angles shallower than nominal were investigated to quantify the relative benefits (if any) that may be obtained from $L/D > 0.24$ as offered by optimized aeroshells. The half corridor width between nominal and overshoot trajectories from the $L/D = 0.24$ trajectory (3.9575°) was maintained initially for the higher L/D cases. This approach to redefining the nominal flight path entry angle γ allows reduced peak heating (a strong function of entry angle for a given geometry) while retaining the ability to compensate for off-nominal conditions encountered during entry. The trajectories with thus redefined nominal entry angle were optimized first for minimum stagnation point

heating as before. Characteristics of the optimized trajectories are shown in Table 2, and their altitude time histories are shown in Fig. 4. (The reference radius for Fay-Riddell calculations was taken to be 1 meter.) It can be seen that all entries with higher L/D do indeed produce somewhat lower peak stagnation point heating rate and peak dynamic pressure compared with the $L/D = 0.24$ case. Note that these relatively small improvements were achieved despite the higher ballistic coefficients resulting from lower drag at higher L/D . The increase in lift obtained at the higher trim angles permitted by optimized forebody shapes more than compensates for the reduction of their drag, bringing some benefit in terms of (slightly) more benign stagnation point heating, but with somewhat higher stagnation point heat loads.

Table 2 Nominal trajectories optimized for minimum peak Fay-Riddell stagnation point heating

L/D	C_D	Ballistic coefficient, kg/m^2	Entry angle γ , deg	Peak heating rate, W/cm^2	Peak dynamic pressure, Pa	Total heat load, J/cm^2
0.24	1.47	124.8	-15.288	66.8	11,572	3,078
0.27	1.43	128.8	-14.568	64.4	11,014	3,318
0.32	1.37	133.9	-14.388	64.2	10,895	3,393
0.35	1.28	143.3	-14.337	64.5	11,213	3,439
0.39	1.26	145.8	-14.398	65.6	11,346	3,565

**Fig. 4.** Trajectories optimized for minimum peak Fay-Riddell stagnation point heating rate.

2.2 Minimum Peak Stagnation Point Heating Trajectories with 1°-Shallower Entry Angle

A further step was taken next to exploit the greater control authority offered by optimized aeroshells trimmed for higher L/D. The nominal entry angle was further adjusted to be shallower by 1°, leaving at least a 3° corridor width that is still more than adequate to compensate for off-nominal factors likely to be encountered during entry. In addition to minimizing peak Fay-Riddell stagnation point heating, the shallower trajectories were also constrained to decelerate to Mach 2.1 at a higher terminal altitude of 14 km. This type of trajectory simulation has been applied to L/D = 0.24 and 0.35 cases only, as those have a significant difference in L/D values and comparing their performance should give a feel for the relative benefits in heating from the higher L/D offered by the optimized aeroshell. Pertinent characteristics of the optimized trajectories are shown in Table 3, and

their altitude time histories are shown in Fig. 5. As can be seen from Table 3, the differences in peak heating rate and peak dynamic pressure between nominal and shallow entries for L/D = 0.24 are still relatively small, but they are much larger for L/D = 0.35. When the *shallow* entries for L/D = 0.24 and 0.35 are compared, the differences in peak heating rate and peak dynamic pressure are quite significant, with L/D = 0.35 having peak heating rate lower by 12+ % and peak dynamic pressure lower by nearly 27%. Such a result could be explained by the fact that for the L/D = 0.24 shallow entry, the peak stagnation point heating occurs at 86 seconds and at the lower altitude of 33.2 km, compared with 96 seconds and 38.1 km for the L/D = 0.35 shallow case. Likewise, peak dynamic pressure for L/D = 0.24 occurs at 96 seconds and 26.8 km altitude, while the L/D = 0.35 shallow entry experiences its peak dynamic pressure at 124 seconds and 28.4 km. Ambient density in the Martian atmosphere changes exponentially with altitude; thus, the higher altitudes at

which peak heating and dynamic pressure occur for shallow $L/D = 0.35$ entry evidently lead to lower peak values of heating rate and dynamic pressure than those

of the shallow $L/D = 0.24$ entry case in spite of the velocity differences at those peak times.

Table 3 Comparison of min. peak stagnation pt. heating trajectories with nominal and shallow entry angle

Trajectory type	Entry angle, deg	Peak heating rate, W/cm^2	Peak dynamic pressure, Pa	Total heat load, J/cm^2	Terminal altitude, km
Nominal, $L/D = 0.24$	-15.800	69.8	12,125	3,007	10.66
Shallow, $L/D = 0.24$	-14.800	67.0	12,261	3,050	14.26
Nominal, $L/D = 0.35$	-14.337	64.5	11,213	3,439	10.05
Shallow, $L/D = 0.35$	-13.337	58.7	8,977	3,807	13.97

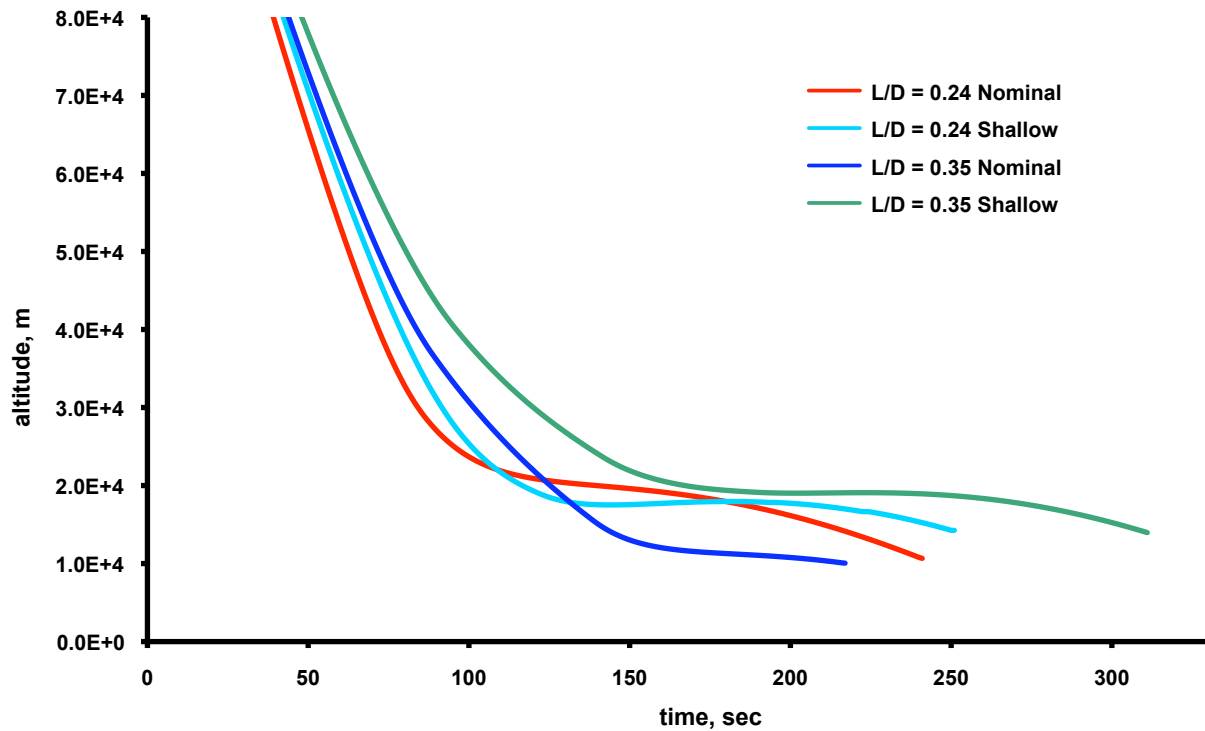


Fig. 5. Comparison of optimized trajectories for $L/D = 0.24$ and $L/D = 0.35$.

2.3 Conclusions from Minimum Peak Stagnation Point Heating Trajectory Optimization

Higher L/D with somewhat lower C_D , offered by an optimized aeroshell in conjunction with non-orthodox design of nominal trajectories, provides several key advantages (admittedly with a somewhat increased heat load as might be expected from the extended entry duration):

1. Reduced stagnation point peak heating rates and peak dynamic pressures as compared with the baseline trajectories ($L/D = 0.24$, $C_D = 1.47$).
2. Potential to shape the entry trajectory in order to delay transition to turbulence by flying at higher altitudes through the phase of maximum dynamic pressure, taking advantage of higher lift coefficients offered by the optimized shape. Thus,

the peak dynamic pressure, which is the primary laminar-to-turbulent flow transition driver, may be significantly reduced or more readily kept below some prescribed critical value. (This aspect is pursued below.)

3. Operational advantages include better ability to perform precision landing in the presence of multiple off-nominal factors, ability to land at elevated locations on Mars, and better cross-range capability to land at alternative sites in case of an emergency or change in mission scenario.

2.4 Nominal Trajectory Optimized for Minimum Peak Dynamic Pressure With an Altitude-Velocity Constraint

The next step in the development of an efficient entry trajectory for the optimized spherical-segment shape

was the implementation of an Altitude-Velocity constraint based on the assumption that as long as the nominal trajectory (flown in the presence of off-nominal factors) does not cross it, the heating environment over [a certain portion of] the heat shield will stay laminar. Since development of such a constraint requires a significant number of high fidelity flow calculations, it is not undertaken lightly for multiple candidates. Therefore, it was decided that the further work would concentrate on a heat shield trimmed at $L/D = 0.39$, rather than at $L/D = 0.35$, in order to use the advantage of higher lift to a fuller extent. This implied increasing the nominal angle of attack from -24° to -26° (still moderate).

As outlined in section 1.3, multiple laminar flow solutions for $L/D = 0.39$ were calculated for a range of velocities and altitudes and used to construct a trajectory constraint in (Velocity, Altitude) space intended to keep momentum thickness-based Reynolds number Re_θ below the critical value of 200 above the apex of the spherical segment, thereby tending to delay transition upstream of that location. In other words, the constraint was developed assuming that the area of transition will not spread below the apex of the heat shield; thus, at least 50% of the heat shield acreage should stay laminar. Furthermore, the entry angle for a new nominal trajectory was chosen to be -11.938° , which still leaves 1.5° to the overshoot boundary; see Table 1. Such a choice was driven by the desire to exploit the advantage of the wider entry corridor provided by the spherical segment trimmed at $L/D = 0.39$. This decision is supported by experience from recent Martian entries [7] where the corridor width between nominal and overshoot trajectories was as small as 1 degree. However, even with the shallow -11.938° entry, some trial trajectories simulated with 70% of nominal atmospheric density were found to cross the constructed Altitude-Velocity constraint, showing that just following the constraint is not necessarily the right approach. Note that the constraint was constructed with a *nominal* atmosphere assumed when the flight conditions for the needed flow calculations were determined, so interpreting *off-nominal* atmosphere results with respect to that constraint is rather confusing.

Instead of minimizing peak stagnation point heating, for the new nominal trajectory it was decided to minimize the peak dynamic pressure in the presence of

the Altitude-Velocity constraint as the trajectory's lower bound. The result of optimizing the nominal-entry-angle trajectory for minimum dynamic pressure is shown as the upper red curve in Fig. 6. Happily, the trajectory's Altitude-Velocity profile essentially mimicked that of the constraint, but it became positioned significantly higher, with the average distance between them being around 5 km. It may be wondered why the new constraint was not active in the optimized trajectory, but recall that the constraint is somewhat arbitrary in that the heat shield apex (center) was taken to be the reference point where Re_θ was required not to exceed 200. The reserve in altitude thus predicted (for laminar flow over about 50% of the acreage) provides a good margin that should tend to keep off-nominal trajectories from violating the altitude-velocity constraint.

Another approach to easing aerothermal environments might be to design a nominal trajectory with shortest flight time, which is roughly equivalent to minimizing the integrated heat *load* at the stagnation point. In this case, to shorten such a trajectory flight time, a nominal entry angle in the middle of the entry corridor should be used to achieve a steeper entry. Thus, for $L/D = 0.39$ with mid-corridor entry angle of -14.398° , such a trajectory optimization was performed and its resulting altitude and dynamic pressure time histories are compared in Fig. 7 with those of the minimum-peak-dynamic-pressure trajectory. The duration of the minimum-stagnation-point-heat-load trajectory is less than half that of the minimum-dynamic-pressure trajectory. Table 4 shows that its integrated heat load is correspondingly lower, while the peak stagnation point heating is about 50% higher.

However, the maximum dynamic pressure for the minimum-heat-load trajectory is about five times higher than that of the minimum-dynamic-pressure trajectory, which has an entry angle of -11.938° . As one might expect, the shorter trajectory violates the Altitude-Velocity constraint throughout the whole range of altitude where it is defined, as seen in Fig. 6. It is reasonable to conclude that for the minimum-heat-load trajectory the vehicle will transition early to turbulent flow over much of the acreage, meaning it will accumulate a (stagnation point) heat load that in reality will be higher by a factor of three to six than the laminar prediction of about $3,000 \text{ J/cm}^2$.

Table 4 Parameters of trajectories optimized for min. dynamic pressure and min. stagnation pt. heat load

Trajectory Type	Atmos. density, % of nom.	Entry angle, deg	Angle of attack, deg	Drag coeff., n/d	Lift coeff., n/d	Max. dynamic pr., Pa	Max. stag. pt. heat flux, W/cm^2	Integrated heat load, J/cm^2
Min. Dynamic Pressure	100	-11.938	26	1.2582	0.4933	4,522	49.72	4,952
Min. Heat Load	100	-14.398	26	1.2582	0.4933	23,462	76.98	3,042

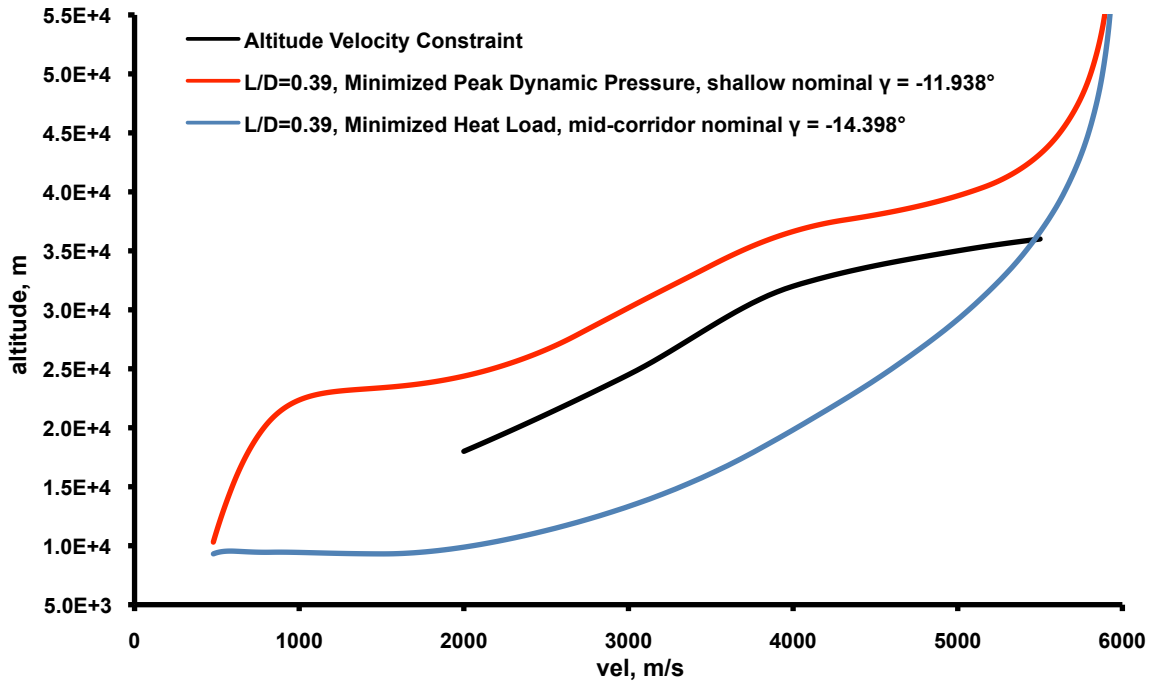


Fig. 6. Altitude-velocity diagram for the constraint and for nominal trajectories optimized for minimum peak dynamic pressure and minimum integrated stagnation point heat load with $L/D \approx 0.39$ and $C_D \approx 1.22$.

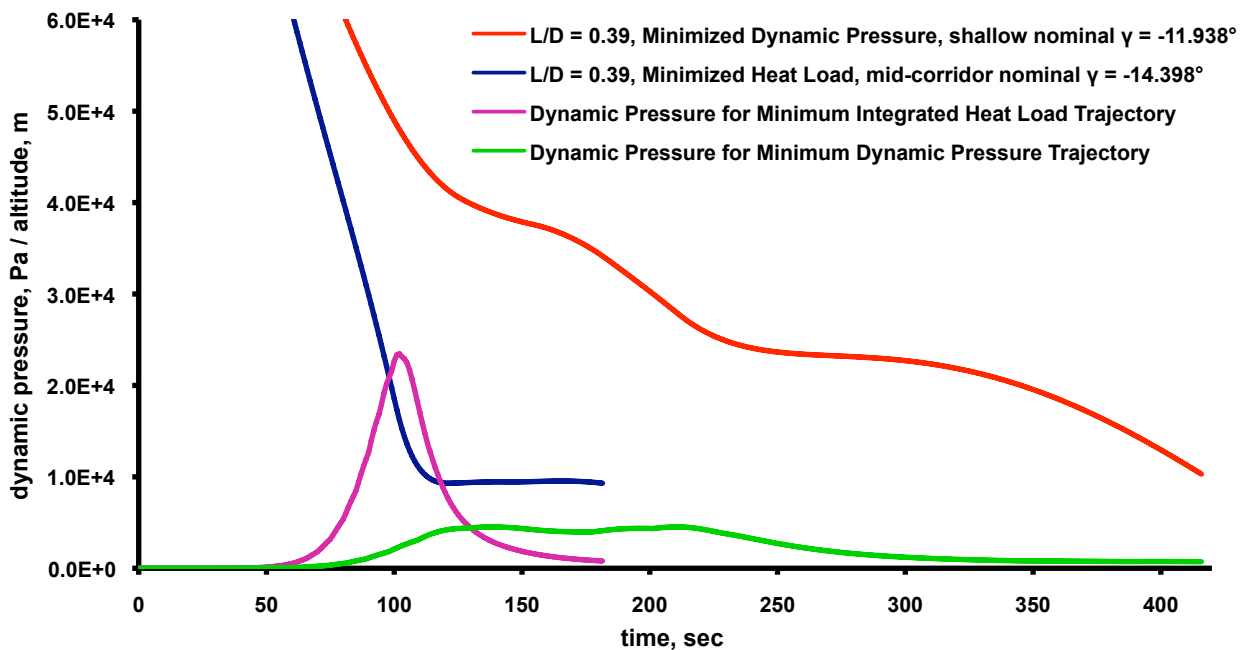


Fig. 7. Altitude and dynamic pressure time histories of nominal trajectories optimized for minimum stagnation point heat load and minimum peak dynamic pressure.

While both optimized trajectories targeted the same end conditions (Mach 2.1 above 10 km altitude), unlike the minimum-heat-load trajectory with its single peak in dynamic pressure occurring at 102 sec, the minimum-dynamic-pressure trajectory has two dynamic pressure peaks with similar magnitudes of about 4,500 Pa, occurring at 140 sec and at 213 sec (green lower curve in Fig. 7). Between these two peaks, the dynamic pressure profile remains nearly flat. This comparison demonstrates how minimizing peak dynamic pressure tends to “spread” dynamic pressure

over much longer flight times, thus keeping its magnitude lower and potentially delaying transition to turbulence over the relevant portion of the heat shield.

In view of its favorable performance with respect to the Velocity-Altitude constraint, this minimum-dynamic-pressure trajectory with nominal $\gamma = -11.938^\circ$ was settled on as the reference for dispersion studies as discussed next.

2.5 Robustness of Nominal Optimized Trajectory

To test the robustness of the nominal trajectory optimized for minimum peak dynamic pressure, it was re-simulated in the presence of multiple off-nominal factors applied to the nominal flight conditions. The altitude-time histories of these off-nominal trajectories are presented in Fig. 8. The combinations of simulated dispersions included $\pm 30\%$ of nominal atmospheric density (figure legend ρ), $\pm 0.25^\circ$ error in the nominal entry angle (legend γ), and $\pm 2^\circ$ error in control of the vehicle's trim angle (legend α), with the magnitudes representing limiting values presently expected for Mars entry. These off-nominal factors were purposely combined in such a way as to exacerbate the entry environment. For example, 70% of nominal density was combined with 0.25° shallower entry angle and with -28° angle of attack, which results in a lower drag

coefficient of 1.1954. The other off-nominal cases were combined in similar ways as well. Together, they serve to represent a plausible envelope of uncertainty for the nominal optimized trajectory.

Table 5 describes how off-nominal conditions were combined in simulated trajectories, and compares their results with those of the nominal trajectory. Simulations with combined off-nominal factors produced relatively small dispersions in maximum dynamic pressure, heating rate and integrated heat load compared with the nominal trajectory. Thus, the biggest increase in peak dynamic pressure is just 5% over the nominal, the maximum off-nominal heating rate is about 3% higher than the nominal, and the highest integrated heat load is 13% larger than the nominal value.

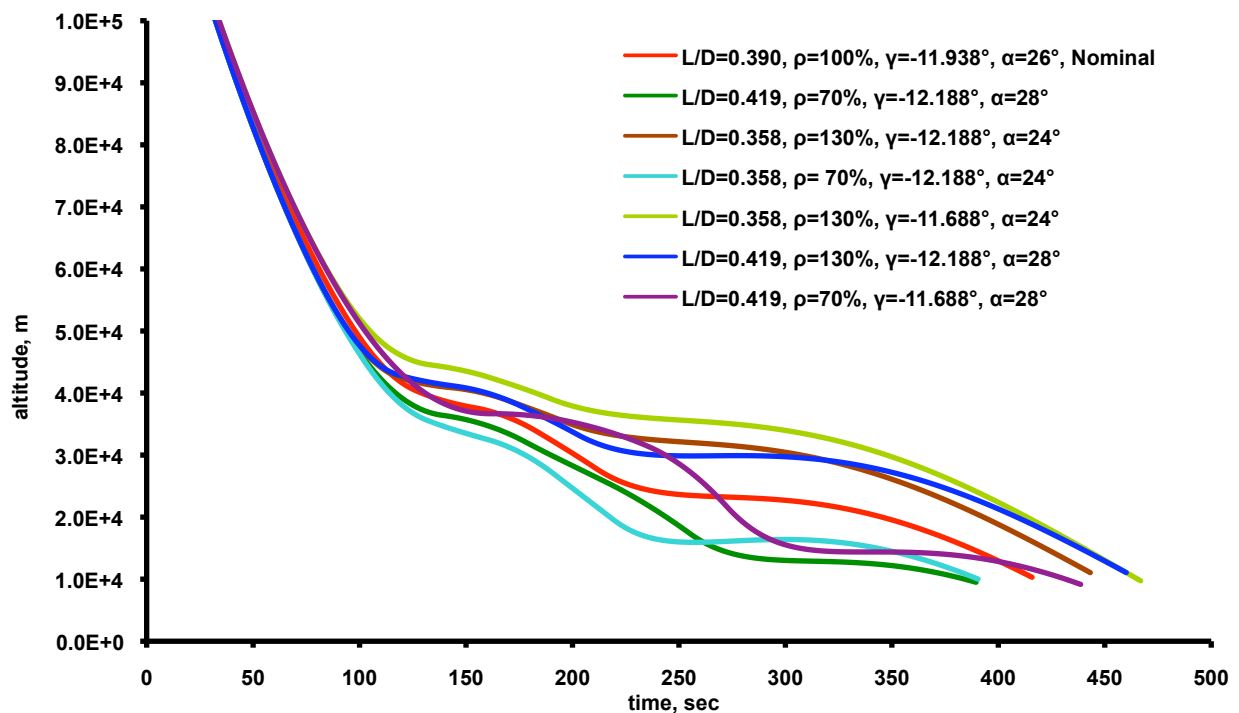


Fig. 8. Altitude time histories for off-nominal trajectories, suggesting an envelope of uncertainty.

Table 5 Parameters of selected simulated off-nominal trajectories

Trajectory L/D	Atmos. density, % nominal	Entry angle, deg	Angle of attack, deg	Drag coeff., n/d	Lift coeff., n/d	Max. dynamic pr., Pa	Max. stag. pt. heat flux, W/cm ²	Integrated heat stag. pt. load, J/cm ²
0.390, nominal	100	-11.938	-26	1.2582	0.4933	4,522	49.72	4,952
0.419	70	-12.188	-28	1.1954	0.5012	4,416	49.21	5,190
0.358	130	-12.188	-24	1.2968	0.4642	4,549	50.23	4,900
0.358	70	-12.188	-24	1.2968	0.4642	4,763	50.22	4,710
0.358	130	-11.688	-24	1.2968	0.4642	3,498	45.74	5,350
0.419	130	-12.188	-28	1.1954	0.5012	4,512	51.02	5,140
0.419	70	-11.688	-28	1.1954	0.5012	4,470	46.38	5,600

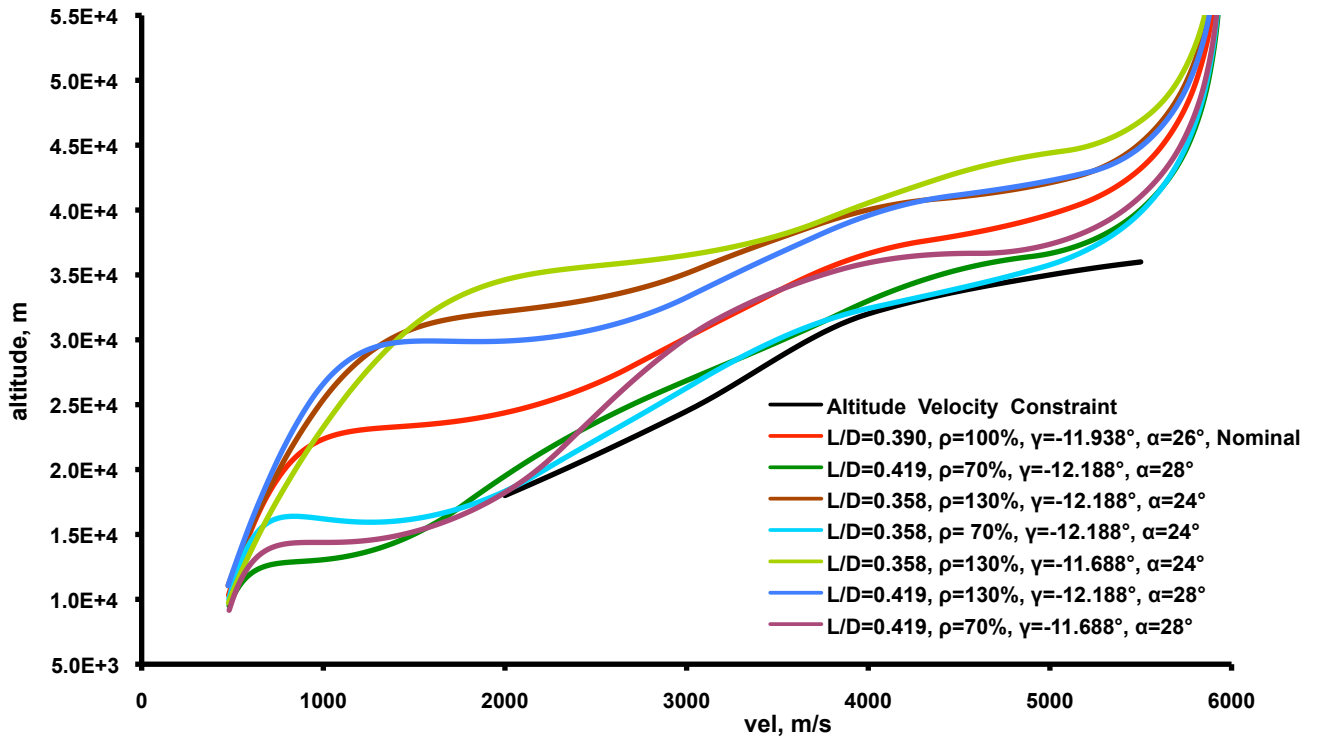


Fig. 9. Altitude-Velocity profiles for simulated off-nominal trajectories.

As seen in Fig. 9, all off-nominal trajectories have their Altitude-Velocity profiles above the constraint, which is shown as the short black curve. Note that the three profiles that touch the Altitude-Velocity constraint represent off-nominal cases with $\pm 30\%$ of nominal

atmospheric density, simulated among other off-nominal factors. The peak dynamic pressures of these cases are still significantly lower than that for the Altitude-Velocity constraint, which is based on nominal atmospheric density; see Fig. 10.

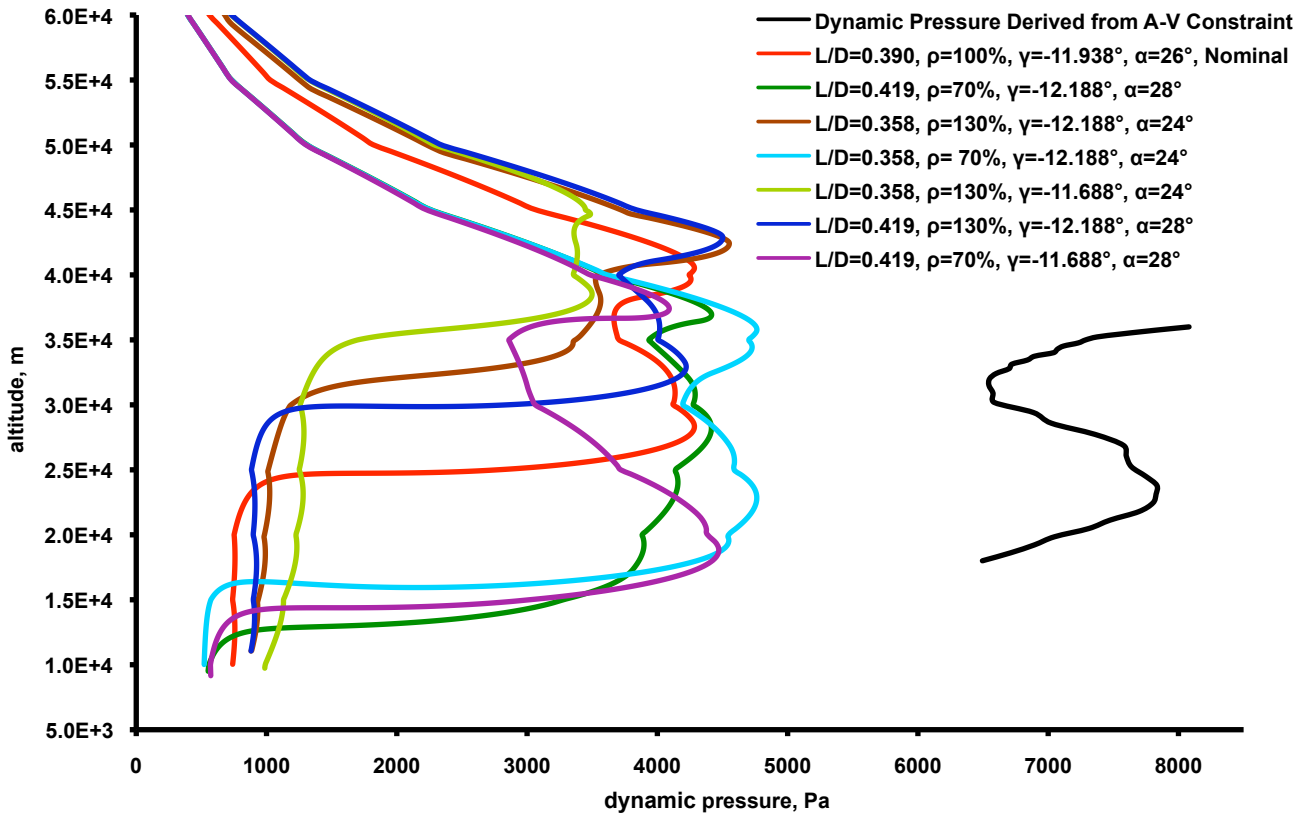


Fig. 10. Dynamic pressure profiles for simulated off-nominal trajectories, and Altitude-Velocity constraint.

Observation of results from these off-nominal trajectories leads to a potentially important conclusion: all values of maximum dynamic pressure are below 4,800 Pa, which is significantly lower than the limit of about 6,500 Pa set by the Altitude-Velocity constraint; see Fig. 10. Originally, this constraint was developed assuming that the zone of turbulent transition will not spread beyond the apex of the heat shield; i.e., at least 50% of the heat shield acreage will stay laminar. However, with the demonstrated maximum dynamic pressure values (resulting from very demanding off-nominal trajectories) being below 4,800 Pa, it may well be that the portion of the forebody acreage retaining laminar flow would be higher than 50%.

CFD calculations of the aerothermal environment for the off-nominal trajectory with the highest peak dynamic pressure of 4,763 Pa, shown as cyan fourth

from the bottom in Fig. 10, were performed to check this conclusion. The resulting laminar and turbulent heat flux and laminar Re_θ distributions for the peak stagnation point Mach 25.55 point on the trajectory are shown in Fig. 11. As predicted, Re_θ is below 200 over more than half the heat shield (as it is also in the peak dynamic pressure Mach 23.51 solution not shown). However, the turbulent flow solution appears to be inconsistent with Re_θ predictions. The SST model with its own criterion for transition produces turbulent flow for about 75% of the acreage, not 50%. Along the shoulder, where Re_θ tends to increase more slowly than on the acreage, the turbulent heating is higher as might be expected from the higher curvature. Lee-side turbulent bump factors of about 2 are evident in the centerline heating of Fig. 12. The nominal Mach 24.3 solution for MSL shows much higher bump factors.

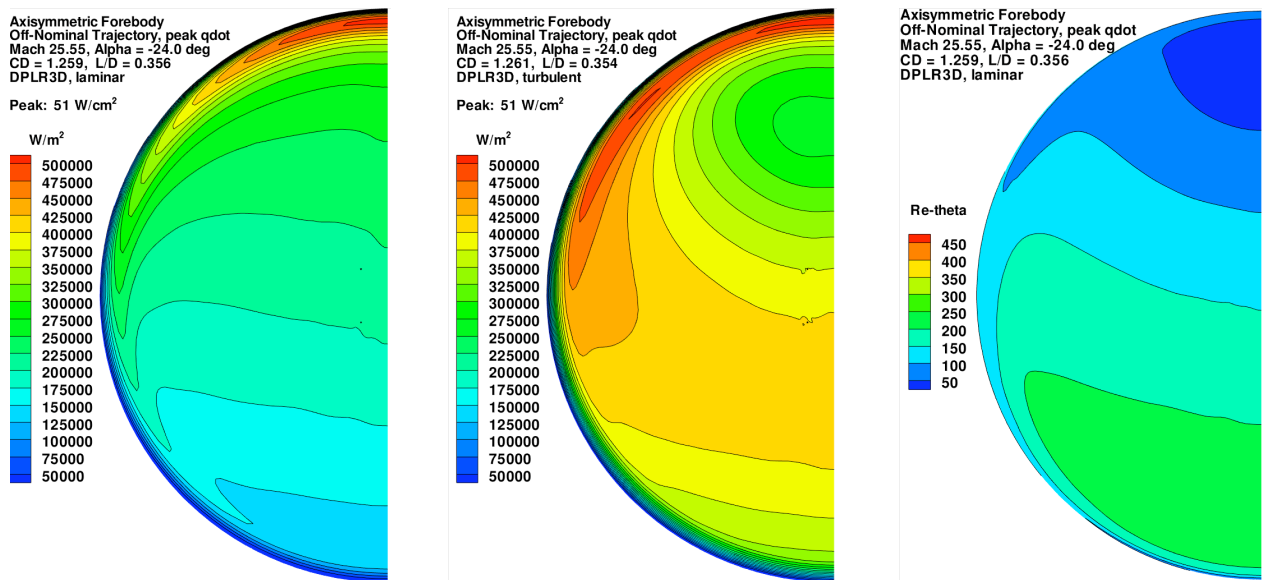


Fig. 11. Laminar and turbulent surface heat flux and laminar Re_θ at the peak stagnation point heating point on the worst-case off-nominal trajectory calculated (Mach 25.55, $\alpha = -24^\circ$, 70% nominal density, $L/D \approx 0.35$).

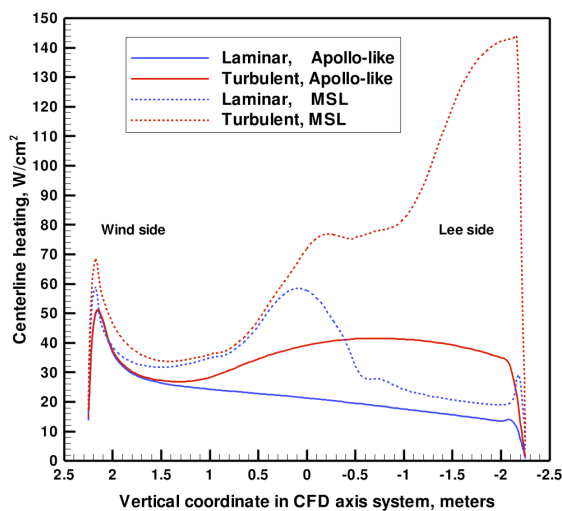


Fig. 12. Centerline heating distributions.

It appears that the strategy of constructing an Re_θ -based trajectory constraint is rather tenuous, at least in this instance. (Note that the boundary layer edge Mach number is subsonic in these solutions, so use of Re_θ/M_{edge} is not the answer either.) Moreover, it may have been better to construct the constraint in density-Velocity space, not Altitude-Velocity space, so it would not be restricted to the nominal atmosphere.

Nevertheless, these results demonstrate determination of a flexible, robust trajectory for an MSL-class vehicle that is preferable to the 70° sphere/ cone in terms of turbulent heating, and has proven aerodynamic stability based on Apollo experience, which presumably translates to Mars entry. The benefits of Apollo-like higher L/D , reasonably high C_D , and shallow entry surely outweigh the inevitable increase in heat load compared with steeper entries. Application to heavier entry vehicles appears worthy of investigation.

3. SUMMARY AND CONCLUSIONS

A methodology has been presented for developing optimized MSL-class entry trajectories that should encounter significantly less severe aerothermal heating environments than the traditional 70° sphere-cone. A different heat shield shape with higher L/D is implied, and a preparatory shape optimization study by the authors concluded that the simple spherical-segment configuration of Apollo and CEV is hard to beat. Some better blending of curvature at the shoulder came out of the initial shape optimization, but its effect on shoulder heating is *not* significant according to CFD comparisons (not shown here), meaning results effectively apply to the Apollo forebody scaled to 4.5 meters in diameter.

For $L/D = 0.24$ (MSL), 0.27, 0.32, 0.35, and 0.39, and somewhat shallower entry angles nearly 4° from overshoot, optimized trajectories were first calculated to minimize peak stagnation point heating. This was found to be of limited benefit, so the nominal trajectory was reoptimized to minimize peak *dynamic pressure* in combination with entry angles 1° shallower (still conservative). For $L/D = 0.35$, this produced significant reductions in both the peak stagnation point heating and the peak dynamic pressure. Raising L/D to 0.39, the entry angle was further reduced to allow just 1.5° margin from overshoot, and an Altitude-Velocity constraint was introduced based on Re_θ from 15 *DPLR* solutions with Alpha -26° for that L/D . On the resulting nominal minimum-peak-dynamic-pressure trajectory, the peak stagnation point heating at Mach 26.22 was calculated by *DPLR* to be 57 W/cm² on the windward shoulder and 43 W/cm² or less for the acreage. For comparison, according to comparable *DPLR* solutions at a nominal peak stagnation heating point for MSL (Mach 24.3, Alpha -16.22°, C_D 1.460, L/D 0.249) the peak laminar heating is about 55 W/cm² (on the nose) and the peak turbulent heating reaches 144 W/cm² on the down-stream outer portion of the cone.

The robustness of the nominal optimized trajectory was demonstrated by reoptimizing it in the presence of multiple dispersions in atmosphere density, entry angle, and angle of attack (i.e., L/D). The Altitude-Velocity constraint was shown not to be violated by any of the off-nominal trajectories, suggesting that the intent of delaying turbulent transition over the upper half of the heat shield through use of such a constraint appears viable. However, the *DPLR* solutions for the peak stagnation heating point on the worst-case off-nominal trajectory show that turbulent flow appears over about 3/4ths of the acreage, not just half of it.

Still, it is believed that the presented approach can also delay transition if applied to larger Mars entry vehicles, provided that they have similar heat shield configurations and ballistic coefficients around 145-150 kg/m². For example, a 100-MT entry vehicle with spherical segment shape would need to have a diameter of about 26.4 m, raising rigid versus flexible aeroshell issues.

Future heavy Mars landers will almost certainly demand an aerocapture phase with initial entry velocity

higher than 7 km/s. It would likely be too risky to reduce the entry angle to as little as 1° from overshoot as assumed for descent entry. Further work is also needed to determine if there is much scope for establishing an Altitude (Density?)-Velocity constraint to help delay transition over a meaningful portion of the acreage during aerocapture.

It is understood that for such large aeroshells, radiative heating becomes an issue, but for Mars entries below 7 km/sec, radiative heating is expected to be negligible (although concern about infrared radiation from CO₂ and CO at the lower Mach numbers has emerged recently). Even so, reducing nominal convective heating by whatever means should still be beneficial, and an approach has been demonstrated in this work through the combination of choosing a more promising shape and optimizing the trajectory for shallower entry.

ACKNOWLEDGMENTS

The authors are grateful to Evans Lyne and Joshua Johnson for performing the requested *POST II* simulations, to Todd White for scripting initial volume gridding off a surface grid, to Dinesh Prabhu for his advice with the *DPLR* calculations, and for the feedback from reviewers James Brown and Loc Huynh. Sponsorship of this study by the Ames Research Center Aerothermodynamics Branch under NASA Contract NNA04BC25C to ELORET Corporation is also much appreciated.

REFERENCES

1. Jits R. Y. and Saunders D. A., "Aeroshell Shape and Trajectory Optimization," ELORET Report TSA-01-DD3-3-2008, Ames Research Center, April 2008.
2. Schneider S. P., "Summary of Hypersonic Boundary-Layer Transition Experiments on Blunt Bodies with Roughness," Journal of Spacecraft and Rockets, Vol. 45, No. 6, November-December 2008.
3. Brown J. L., "The Effect of Forebody Geometry on Turbulent Heating and Thermal Protection System Sizing for Future Mars Mission Concepts," 4th International Planetary Probe Workshop, 2006.
4. Wright M. J., Candler G. V., and Bose D., "Data-Parallel Line Relaxation Method for the Navier-Stokes Equations," AIAA Journal, Vol. 36, No. 9, 1998.
5. Raiszadeh B. and Queen E. M., "Partial Validation of Multibody Program To Optimize Simulated Trajectories II (POST II) Parachute Simulation With Interacting Forces," NASA/TM-2002-211634, April 2002.
6. Fay J. A. and Riddell F. R., "Theory of Stagnation Point Heat Transfer in Dissociated Air," Journal of the Aeronautical Sciences, Vol. 25, No. 2, February 1958.
7. Braun R. D. and Manning T. M., "Mars Exploration Entry, Descent and Landing Challenges," Paper #0076, IEEE Aerospace Conference, Big Sky, Montana, March 2006.